Aerodynamic forces of interacting spheres representative of space debris re-entry: Experiments in a supersonic rarefied wind-tunnel

Viviana Lago, Vincente Cardona

Version of Record: https://www.sciencedirect.com/science/article/pii/S0094576521005786
Manuscript_a92775dcc1fb65be9a30d0d7ccaa4ea9

Aerodynamic Forces of Interacting Spheres Representative of Space Debris Re-entry: Experiments in a Supersonic Rarefied Wind-Tunnel

Vincente Cardona[a,1,*], Viviana Lago[a,2]

[a]*ICARE, CNRS, 1C av. de la Recherche Scientifique, CS 50060, F-45071 Orléans cedex 2, France*

Abstract

Experimental investigations of two interacting spheres were carried out in a Mach 4 flow with a static pressure of 2.666 Pa. This study was performed in the MARHy wind tunnel, an adjustable supersonic or hypersonic low-density facility. The main purpose is to estimate how the interaction between spherical debris modify the aerodynamic forces during their atmospheric entry. Indeed, around 80 km, altitude experimentally reproduced thanks to MARHy flow conditions, most debris fragment. The multiple debris, resulting from fragmentation, interact with each other's, which may impact their trajectory. The purpose of this work is to analyze the behavior of a moving sphere placed in the wake of another one. The moving sphere is suspended with two thin wires, so it can almost freely move in the flow direction and physically respond to the acting flow forces of the wake of the first one. Aerodynamic forces are then calculated from the sphere angle deflection. The qualitative analysis of the experimental results will be discriminated first with respect to the trajectory of the second sphere, and secondly with respect to the evolution of the aerodynamic forces according to the sphere.

Keywords: Shock/shock interactions, Supersonic rarefied flow, MARHy wind tunnel, aerodynamics

Nomenclature

α	Angle of the wire (°)
λ	Mean free path (m)
μ	Dynamic viscosity (Pa.s)
ρ	Density (kg.m^{-3})
ς	Similarity number
C_d	Drag coefficient
D	Sphere diameter (m)
$\vec{F}$	Force endured by the second sphere (N)
g	Gravitational acceleration = 9.81 m.s^{-2}
Kn	Knudsen number
m	Mass of the second sphere
Ma	Mach number
p	Pressure (Pa)
$\vec{P}$	Weight of the second sphere (N)
Re	Reynolds number
R_m	Specific gas constant = 287.058 m^2.s^{-2}.K^{-1}
S	Reference area (m^2)
$\vec{T}$	Tension force of the wire (N)
Te	Temperature (K)
U	Flow speed (m.s^{-1})

Subscript

∞	Free-stream conditions
0	Stagnation conditions
1	First sphere (fixed)
2	Second sphere (moving)

1. Introduction

The number of man-made debris on Earth orbits is constantly increasing [1]. Problem is that those debris will eventually re-enter the atmosphere. Among the multitude of them, smallest debris are prone not to survive as a consequence of thermal loads [2]. But larger debris, depending on their shape and materials, can pass through a major part of the upper atmosphere, and eventually reach the ground. If they do so, the impact creates environmental damage and sometimes it can lead to human casualties, given the large populated area [3]. As important debris recently re-entered Earth's atmosphere, we already have an idea of this growing problem. As an example, the impact area and time of debris from the Long March 5B rocket, which crashed on May 9th 2021, were not sufficiently accurate to prevent early enough serious consequences, if any. Indeed, space debris, which are uncontrolled structures, are not designed to re-enter the atmosphere; the knowledge of their behavior during their return to Earth is thus to be studied.

While re-entering the atmosphere, space debris evolve at hypersonic velocities. As their altitude diminish, the density of air molecules increases. Consequently, space debris will undergo four different flow regimes as they approach Earth's surface: free-molecular, transition, slip-flow, and continuum regime.

⋆Aerodynamics of interacting spheres
*Corresponding author
[1]PhD Student: vincente.cardona@cnrs-orleans.fr
[2]Leader of the FAST team: viviana.lago@cnrs-orleans.fr

With increasing density, dynamic pressure and heat flux increase too, leading, most of the time, to debris fragmentation. This phenomenon occurs generally in transition and slip-flow regimes, at altitude ranging between 91 and 50 km [4, 5] depending on the size, shape, materials and velocity of debris. As a result of the fragmentation, one debris becomes a multitude of smaller debris, interacting with each others, at least on their first instants of existence. Depending on the scenario of their flights, some debris may stay on the wake of other ones, being preserved from the flow and consequently from ablation; or on the contrary, some can suffer thermal loads produced when surfing on the shock wave of a first one, being disintegrated before reaching the ground.

Unfortunately, the real behavior of fragments, when re-entering the atmosphere, is still not well known. When debris interact with each-others, their trajectory can be modified, which adds a supplementary difficulty to calculate accurately the time and area of impact on Earth's surface [6, 7]. Indeed, rarefied regimes, which mostly corresponds to break-up altitudes, still need to be better known. Some experimental works are still focused on the study of the flow around simple geometry [8] to better characterize shock wave shapes and aerodynamic forces in order to improve the knowledge of early stage of atmospheric re-entry. Adding interaction situation to low density effects will allow to determine aerodynamic parameters at the very first moment after fragmentation, and consequently help to understand the behavior of the multiple fragments. With time, it will serve to better predict re-entry trajectory.

Proximal bodies behavior is a highly studied topic. In particular, studies have been focused on the study of a sphere flying in the wake of an other one.

In a continuum regime, sometimes in low density conditions, supersonic and hypersonic studies showed the importance of Edney's shock/shock interferences [9] on pressures and heat flux distribution at the surface of a following object [10, 11, 12, 13]. The consequences on these interferences has also been studied in terms of aerodynamic coefficients [14],[15]. In any case, it has been shown that forces induced during a shock/shock interference strongly impact the trajectory of an object in the wake of a first one [16, 17, 18].

In a rarefied regimes, where shock waves are thicker and more diffuse, shock/shock interferences behavior is different from the continuum regime [19, 20]. To our knowledge, very few results are found in the literature concerning the pressure and heat flux distributions [19, 21] or the aerodynamic forces [22, 23] induced by these interactions in rarefied flows.

In effect, the low density condition creates a flow that no longer can be described by the Navier-Stokes equations, but with the mathematical model of the Boltzmann equation. Numerically, Bird [24] first integrated this model in the Direct Simulation Monte Carlo (DSMC). Slip conditions and accommodation coefficients, in particular for the estimation of aerodynamic coefficients, are points that still need to be better characterized. In order to improve the accuracy of the numerical results, it is interesting to build experimental database, in particular concerning the shock/shock interferences topic.

Unfortunately, wind-tunnels able to recreate flow conditions of high altitudes in terms of pressure are not very common. Such a supersonic or hypersonic rarefied flow can be found at the Princeton University [25], at the German Aerospace Center [26], at the Imperial College [27], at the University of Oxford [28], at the Institut of Theoretical and Applied Mechanics [29] and at the Institut de Combustion, Aérothermique, Réactivité et Environnement, where the present work has been realized.

This paper presents an experimental investigation carried out in the MARHy wind tunnel to explore the interaction of two spheres in a rarefied flow at Mach 4. The experiment consists in analyzing the behavior of a moving sphere placed in the wake of another one with the same diameter. The moving sphere is suspended with two thin wires to a movable support and displaces itself according forces it perceives. Analyzed results will be focused on how shock/shock interferences can affect the trajectory of a sphere in the wake of another.

2. Experimental setup

2.1. The MARHy wind tunnel

This experimental work was carried out in the MARHy wind tunnel, anciently called SR3. MARHy, one of the three wind tunnels of the FAST platform of ICARE, CNRS (France), can reach subsonic to hypersonic velocities in a low density medium.

This facility is composed of three main chambers, as shown in Figure 1. The settling chamber serves to establish stagnation conditions. At the inlet, a valve allows to regulate its static pressure. Experiments are carried out in the test chamber, where free stream conditions are set according to the stagnation conditions, the nozzle used and the pumping conditions. The third chamber is the diffuser, which is connected to the pumping group, composed with 14 Roots type pumps, and 2 primary type pumps.

In the MARHy wind tunnel, the flow can reach a large range of speed and pressure thanks to its numerous nozzles. The test gas depends on the nozzle used: air for Mach numbers lower than 4, and dinitrogen in hypersonic flow for Mach number up to 20. The diameter and length of the isentropic core also depends on the nozzle used. For each one, the flow in the isentropic core is laminar and continuous, meaning that the free stream conditions are perfectly known. The powerful pumping group allows to sustain the operating conditions in continuous and stable conditions with no limitation time.

2.2. Flow conditions

The purpose of the experiment is to provide some answers concerning changes on trajectories of two debris interacting with each other, right after the fragmentation of a parent debris. According the approximate altitudes of fragmentation when a debris enter the atmosphere, it is experimentally wished to obtain a level of rarefaction equivalent to the one at concerned altitudes.

This rarefaction level is characterized with the mean free path

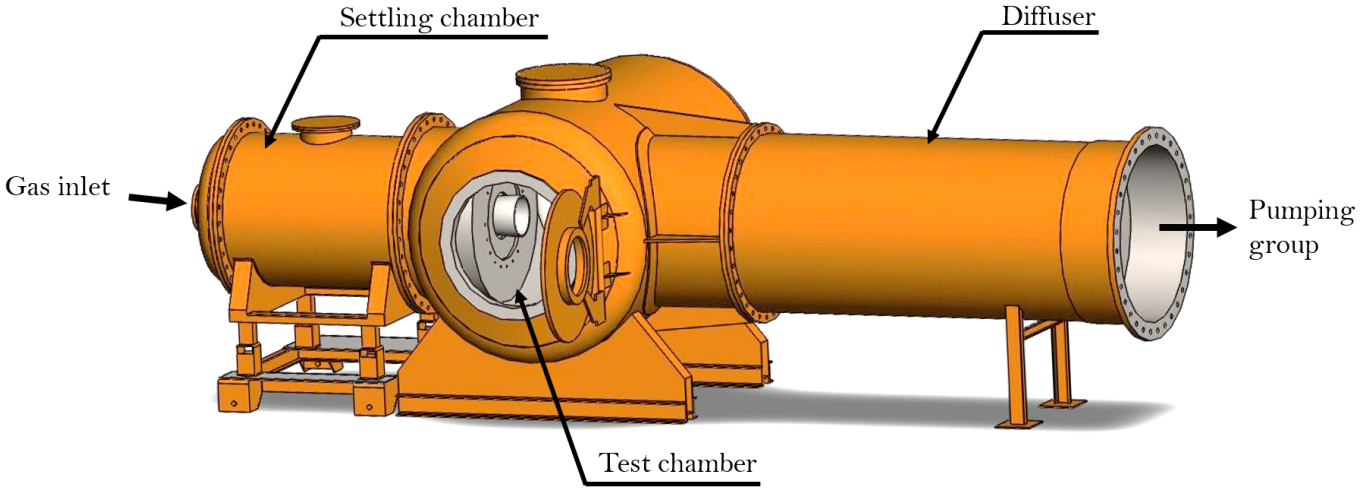

Figure 1: Schematic of MARHy wind tunnel

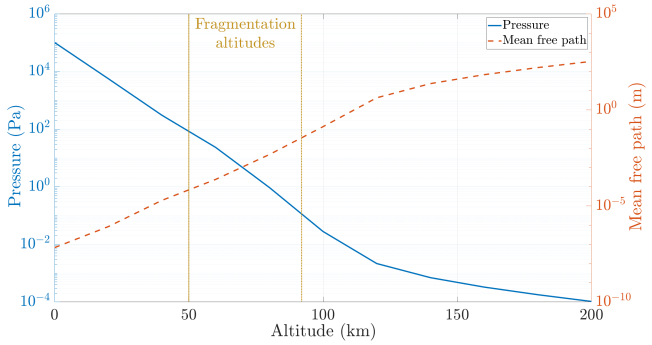

Figure 2: MSISE-90 Model of Earth's upper atmosphere: pressure and mean free path according the altitude.

λ_∞, estimated assuming a variable cross-section hard sphere (VHS) model that appears to be the most employed [30]). This parameter is calculated with Equation 1, where ω_∞, given by the viscosity power law of Sutherland, is 0.92 in this experiment.

$$\lambda_\infty = \frac{\mu_\infty}{\rho_\infty \sqrt{2R_m T_\infty}} \frac{2(7-2\omega_\infty)(5-2\omega_\infty)}{15\sqrt{\pi}} \tag{1}$$

If working with the size of the model (where D_1, the diameter of the first sphere), the Knudsen number Kn_∞, as expressed in Equation 2, is a similitude parameter commonly used to define the rarefaction level.

$$Kn_\infty = \frac{\lambda_\infty}{D_1} \tag{2}$$

According the MSISE-90 Model presented on Figure 2, at estimated fragmentation altitudes between 91 and 50 km, pressure respectively ranges between 0.1 and 100 Pa, while the mean free path ranges between 3.10^{-2} and 7.10^{-5} m.

Not a single ground-based facility is able to reproduce such a rarefied hypersonic flight. It is very hard to experimentally obtain simultaneously all the flight parameters of a debris at fragmentation altitudes.

Nevertheless, it is possible to study independently analogous rarefaction effects in wind tunnels. For this purpose, it is therefore necessary to obtain appropriate Mach and Reynolds numbers. In effect, rarefaction level can furthermore be characterized by the similarity number, also called viscous parameter, which only depends on those two dimensionless numbers, as seen in Equation 3.

$$\varsigma = \frac{Ma_\infty}{\sqrt{Re_\infty}} \tag{3}$$

As Knudsen number is a 'static' similitude parameter only depending on gas density, the viscous parameter is a dynamic similitude parameter because it includes the Mach number and the viscosity. Space debris that enter a large part of the atmosphere and are a potential threat for life on Earth, are mostly larger than 10 cm. Considering a 1 m-diameter main fragment, Prevereaud *et al.* [5] calculated its velocity according the fragmentation altitude, leading to the viscous parameter. Between 78 and 70 km in altitude, it is respectively ranged between 0.293 and 0.130.

On the present investigation we wanted to reproduce similar viscous parameters. For this purpose, the nozzle used is the Mach 4 – 2 Pa which flow conditions are detailed in Table 1, where subscript $_o$ and $_\infty$ correspond respectively the nozzle stagnation and the free-stream conditions. The diameter of the isentropic core is 7.5 cm, so models larger than 5 cm-diameter cannot be properly studied. Consequently, we need to re-scale the physics of atmospheric re-entry. Our main fragment is a 16 mm-diameter sphere as described in 2.4. Free-stream conditions, for our experimental flow, gives $\varsigma = 0.233$ and $Kn = 0.0139$. So, the chosen nozzle ensures to reach a coherent level of rarefaction with what expected at break-up altitudes.

Stagnation and free-stream conditions are respectively obtained experimentally adjusting the static pressures in the settling chamber and in the test chamber (see Figure 1). A micro-valve regulates very accurately the inlet ambient pressure in the settling chamber to stabilize the static pressure. The free-stream pressure is obtained commissioning the number of

Table 1: Flow conditions of the Mach 4 - 2.666 Pa nozzle

Stagnation conditions		**Free-stream conditions**	
gas	ambient air	gas	ambient air
p_o (Pa)	404.792	p_∞ (Pa)	2.666
Te_o (K)	293.15	Te_∞ (K)	69.798
ρ_o (kg.m^{-3})	4.810×10^{-3}	ρ_∞ (kg.m^{-3})	1.331×10^{-4}
		μ_∞ (Pa.s)	4.843×10^{-6}
		U_∞ (m.s^{-1})	669.919
		Re_∞ (m^{-1})	1.84×10^{-2}
		Ma_∞	4.0
		λ_∞ (m)	2.23×10^{-4}

Roots type pumps, and adjusting the opening of the butterfly valve located between the diffuser and the pumping group. Pressures are monitored with MKS absolute pressure sensors which full range is in relation with the pressure values to be measured.

By means of accurate set pressure control of the different sections of the wind tunnel, for the entire set of experiment, a mean Mach number of 4.008 ± 0.012 was obtained, which ensures stable flow conditions in terms of velocity and density.

2.3. Flow-field visualization

In a rarefied flow, the density does not allow to use visualization techniques commonly used in fluid dynamics experiments. The number of particles is so low that no changes in optical index can be observed. As a result, PIV, Schlieren, or other optical technique based on optical index changes do not provide any results. Nevertheless, other techniques based on ionization of particles, such as glow-discharge or electron gun, work on low density flows [31].

For this work, we used the glow-discharge technique generating an electrical discharge through a copper ring placed around the flow, at the outlet of the nozzle, as it can be observed in Figure 3 and Figure 4. A negative voltage of -1 kV is set on this copper ring, inducing a current of 4 mA. As the electrical power is lower than 10 W, the ionization created does not modify the nature of the flow, as shown by Coumar & Lago [32].

This ionization makes the flow visible around models. The luminous intensity varies with the local density of gas molecules. The denser the flow is, the more the luminosity is intense. As a result, since a shock wave is a compression of the medium, it is denser (and brighter) than the free-stream flow. Consequently, the luminosity allows to distinguish shock-waves.

However, this method is a volumetric enlightening, so the luminous intensity of images is the result of integrated intensity values along the line of sight of the camera. So this method does not allow to obtain the local density of the flow-field along the Y-axis.

2.4. Experimental configuration

For this study, as seen in Figure 3 and Figure 4, a first sphere (S_1) is placed in the wind tunnel, in the plane $(X;Z)$ at $Y = 0$ of the nozzle. It represents a parent debris flying in the free-stream conditions given in Table 1; while a second sphere S_2, plays the role of a fragment following the parent debris. S_1 is held in its position with a vertical support which does not create flow obstruction. The support is held in place with a rotary system that allows the sphere to be removed from the flow for background image recording. The first sphere is not aligned in the plane $Z = 0$ on purpose. In effect, the core of the nozzle is 7.5 cm-diameter, so if S_1 was located on the center line of the flow, the displacement area for the second sphere (S_2) would be not enough to explore at least the six types of shock/shock interferences (SSI) as observed by Edney [9]. In order to increase the displacement area of S_2, S_1 has been positioned 30 mm above the center line of the flow. This location does not significantly modify the shock wave of the sphere as previously shown by Cardona *et al.* [20]. As S_1 won't move during the entire experiment (except when recording background images), it is chosen to set its center as the origin of the spatial coordinates system.

S_2 positioning is included in the $(X;Z)$ plane of the nozzle, as for S_1. Its X and Z coordinates are variables discussed thereafter. Its supporting system depends on the type of experiment as explained in 2.4.1 and 2.4.2.

In any case, both models used are 16 mm-diameter spheres in Polyoxymethylene, with a mass of 2.88 g. They have been colored with a thin layer of black spray paint to increase the contrast and improve the iCCD visualization.

Two types of experiments have been realized to investigate the aerodynamic behavior of the secondary sphere.

The first experiment consists in letting a sphere (secondary debris) swing behind a first fixed sphere (parent debris), in order to analyze aerodynamic forces that it undergoes.

The second experiment allows to deepen the analysis of the first one. Indeed, during the almost free movement of the following sphere, different locations have been identified as remarkable. These positions of interference between the two spheres were reproduced, this time with two fixed spheres, allowing a better visualization of the interaction phenomena.

2.4.1. Swinging sphere experiment

The set-up of the swinging sphere experiment, presented on Figure 3, allows to observe the physical response of S_2 to the flow of its parent debris. S_2 is drilled from side to side on an axis passing through its center. A thin non-elastic wire, of 0.07 mm in diameter, passes through this hole to suspend the sphere. The wire is attached on a support which is placed on a motorized system of tri-axial Cartesian translation. The lengths of the two sides of the wire are equal and the sphere cannot slide on the wire. In effect, we glued them together to avoid any displacement in Y-direction, and observe a two-dimensional movement (in the plane $(X;Z)$) of S_2 viewable by the camera.

Concerning the location of S_2, the only position chosen was the starting point. Once the flow was set, we positioned S_2 aligned right behind S_1 in X-direction. This position is considered as the initial position. After being placed in this position, the robot maintaining the support of S_2 is moved up (in Z-direction) with a constant velocity of 0.8 mm.s^{-1}. As S_2 goes up behind S_1, it also moves following the flow direction.

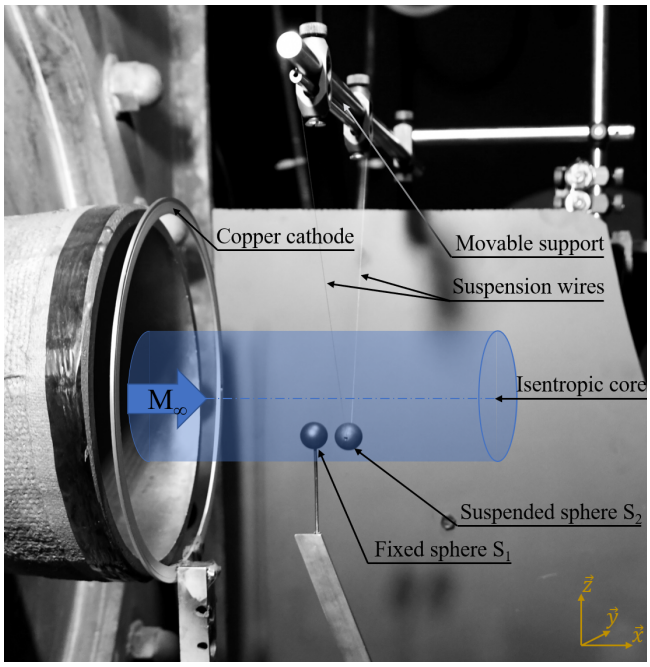

Figure 3: Picture of the swinging sphere set-up

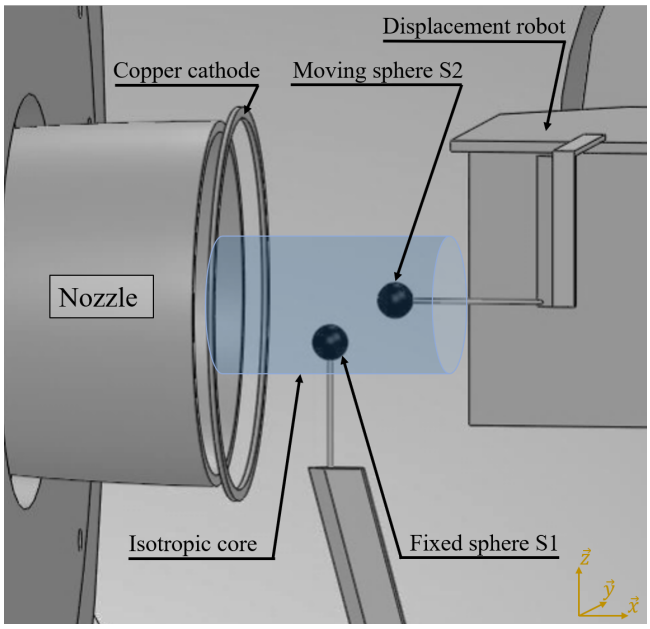

Figure 4: Schematics of the fixed sphere set-up

2.4.2. *Fixed sphere experiment*

Along the trajectory created during the swinging sphere experiment, coordinates of S_2 were obtained with the analysis of images. For some positions of the second sphere in relation to the first one, better quality images are needed to determine the shapes of the shock waves of the two spheres and their potential interactions. As the detection of shock waves requires a set of images with spheres in fixed position a new set-up is used to support the sphere S_2 as presented in Figure 4.

The sphere S_1 is let exactly in same position than in the swinging sphere experiment, and its supporting system does not change.

Concerning S_2, it is now supported by an horizontal 2 mm-diameter threaded rod coming from the rear. This rod is maintained in a profiled vertical support and placed on the same motorized translation system than used in the swinging sphere experiment.

S_2 is precisely placed, by moving the translation system in X and Z direction, in order to obtain the desired location.

2.5. *Recorded images*

To visualize the physical phenomena for both experiments, a Kuro CMOS camera with back-illuminated technology is used. It is equipped with a VUV objective lens (94 mm, f/4.1) giving a resolution of 163 μm.px^{-1}.

For the swinging sphere experiment, an exposure time of 20 ms was adopted to acquire one image, and a total of 3000 images were recorded to cover the complete trajectory. The goal was to record not too much images while ensuring a good tracking of S_2 and its wires, avoiding to blur images. These images (see left image of Figure 5) do not allow to detect shock waves well enough, this is why the second experiment with fixed sphere was also carried out. Here, every image will be treated independently.

For the second experiment, each flow-field, depending on the location of S_2, was recorded through a set of 200 images, with an exposure time of 160 ms each. The same record has been done without any sphere in the flow, that will be used as the background images. For each studied relative position, an averaged image is calculated to reduce noise by averaging intensity matrix of all raw images (middle image of Figure 5). Such method can be used since, during the capture of each set of raw images, the flow is continuous and stable, the objects are fixed, and the ionization is constant. As the copper cathode is placed in front of the spheres, a luminous intensity gradient is created along the flow field (*i.e.,* in X-direction). This experimental bias can be corrected by dividing average images by their average background images. These normalized images, shown in right image of Figure 5), are an improved version of raw images but do not modify the physics of the flow observed. They will be used for the detection of shock wave, discussed in 3.1.2.

3. Results and discussion

3.1. *Image processing*

Two different image processing methods have been applied, depending on the type of experiment.

From the swinging sphere experiment, the X and Z coordinates of the stagnation point of S_2 are determined to obtain its trajectory, and the angle of the front wire is needed for the calculation of the forces. Whereas for the fixed sphere experiment, a specific post processing method have been developed for the detection of the thick shock waves occurring in rarefied flows.

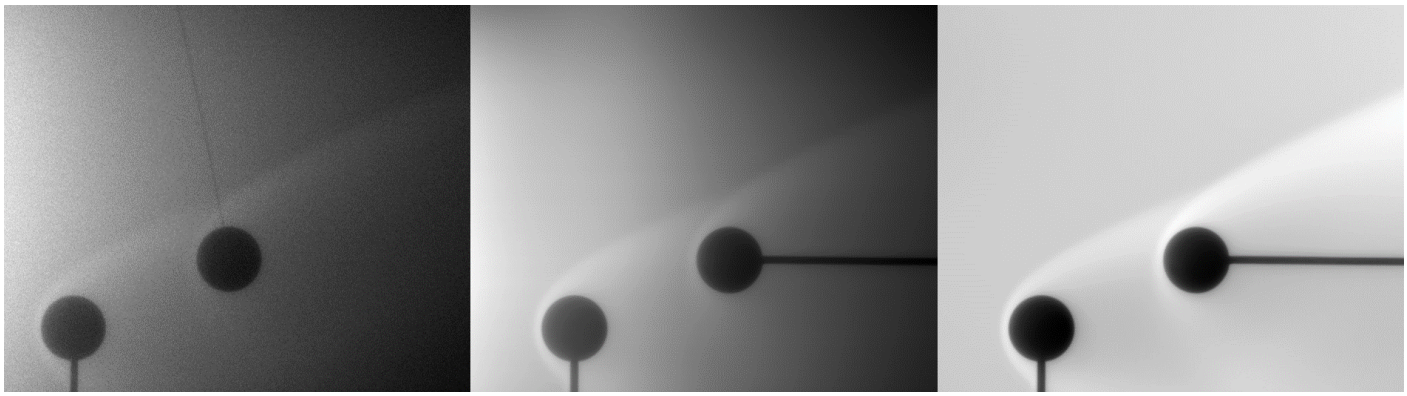

Figure 5: From left to right : single image of the swinging sphere experiment ; average image of a position studied during the fixed sphere experiment ; and its normalized image.

3.1.1. Determination of the angle of the wire

Images obtained during the swinging sphere experiments are similar to the one observed in the left picture of Figure 5. The contour and center of the moving sphere are easily detected with a circle function of Matlab. By means of this tool, the stagnation point of the second sphere is determined with an accuracy of ±1 px = ±0.163 mm.
Nevertheless, the detection of the wire is much difficult because of its small diameter. First of all, it is not possible to detect the wire location with an automatic post processing method since the noise of images is too important, due to short exposure acquisition time, thus the image contrast remains weak. The solution finally considered was a manual approach. The position of the wire was manually located by determining the pixels along the wire. Note that, due to the glow discharge technique, only the front wire is visible, so the determined angle is the angle of the front wire, and this for the whole work. Then, with a simple Pythagore calculation between the center of S_2 and the pointed location of the wire, we deduced the angle of the wire.
Secondly, it is important to determine the position of the sphere S_2 when no flow is on, in order to determine with certainty, the angle of the sphere when the flow is on. The angle of the wire of S_2 without any flow is supposed to be 0°. However, it is not exactly vertical as shown on Figure 6. This means that there is bias due to a slight deviation of the camera alignment. In this figure, X is the measured longitudinal distance between the centers of S_1 and S_2, and α is the measured angle of the wire. As it can be observed, according to the location of the S_2 in the camera field, the angle is not 0°. To rectify this error, we calculated the deviation angle occurring when moving the sphere from the center of the camera field. Equation 4 gives the relation that allows to calculate the real angle from the measured angle.

$$\alpha_{real} = \alpha_{measured} + (X - 25)/50 \tag{4}$$

Considering the error induced by the manual detection of the front wire and the estimation of the initial position, we estimate that the calculated angle is accurate to ±0.4°.

3.1.2. Shock wave detection

The purpose of the second experiment is to improve the visualization of the flow field, and this for the selected cases, along the trajectory described on subsection 3.2, concerned by the interaction between S_1 and S_2. In particular, it is wished to analyze the link between forces experienced by the sphere S_2 and its shock wave shape or the shock/shock interaction that can occur.
The determination of a shock wave around a supersonic or hypersonic object can be achieved analyzing changes in the density flow field. In continuum regime, the delimitation of a shock wave is almost immediate since it is so thin that there is no doubt on its location. But this is not the case when approaching the rarefied regime which induces thick and diffuse shock waves. The delimitation of this kind of shock wave is a major question for different applications on which many researchers still work on [33, 34, 35]. In our case, it is easy to understand why the detection of a shock-wave location is a difficult task. As observed on the top image of Figure 7, the plot of luminous intensity increases softly when approaching the sphere, contrarily to continuum regime [33]. In the stagnation region, the shock appears to be thick, so the delimitation of the shock is not a thin line, but a large region.
As explained in Cardona *et al.* [20], based on the intensity data, we determined the most luminous point corresponding to the denser point, and close to the sphere, we estimated it to be representative of the boundary layer. Then, the middle of shock and the foot of shock are determined, respectively by finding the maximum of the Fourier self-deconvolution and its gradient. This method allows to reduce the noise of images without misrepresenting the physics of the flow.
This method, applied on each horizontal pixel line of images, allows to locate shock waves as shown on the bottom image of Figure 7.

3.2. Trajectory of the swinging sphere

The starting point of the swinging sphere experiment is when S_2 is positioned in its initial position, right behind S_1, as explained in 2.4.1, then the support of the swinging sphere is moved up. Consequently, S_2 displaces itself, almost freely fol-

Figure 6: Pictures of different positions of the sphere for the calculation of the camera deviation angle associated with the measured position of S_2 according S_1 (X) and the measured angle of the front wire (α).

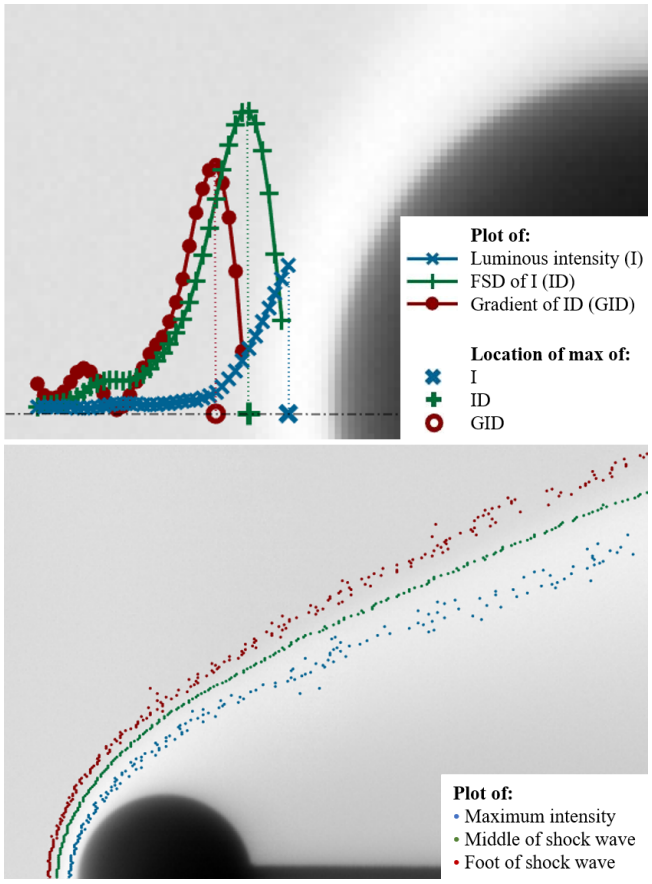

Figure 7: Detection of the shock wave shape of a sphere by Fourier self-deconvolution (FSD) method. Top image : explanation of the process of detection. Bottom image : result of shock detection.

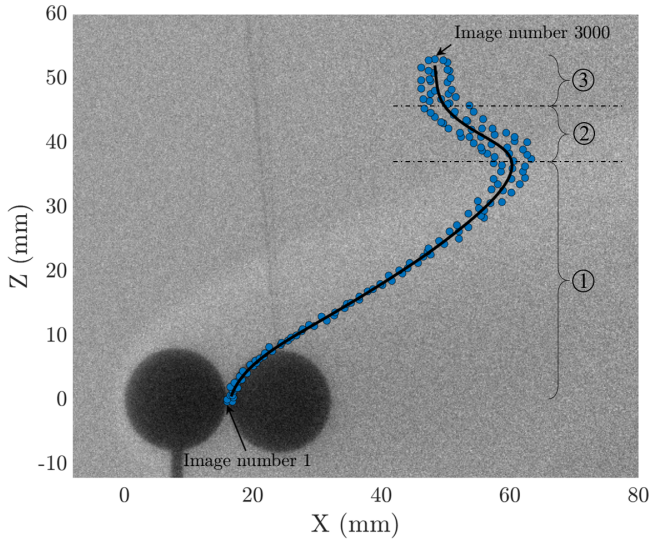

Figure 8: Trajectory of the swinging sphere according the positioning of its stagnation point.

lowing a pendulum movement, in accordance with the forces generated by the flow on the wake of the first sphere S_1. Figure 8 shows the first image of the series and corresponds to the initial position of S_2

Blue points represent the different positions of the stagnation point (SP) of S_2 during its way up. The different positioning of S_2 stagnation point will next be associated to the image number: image number 1 being the initial position, and image number 3000 being the final position. Corresponding X and Z coordinates of S_2 trajectory are plotted on Figure 9.

The analysis of the trajectory presented on Figure 8 has allowed to decompose the movement of S_2 in three main behaviors.

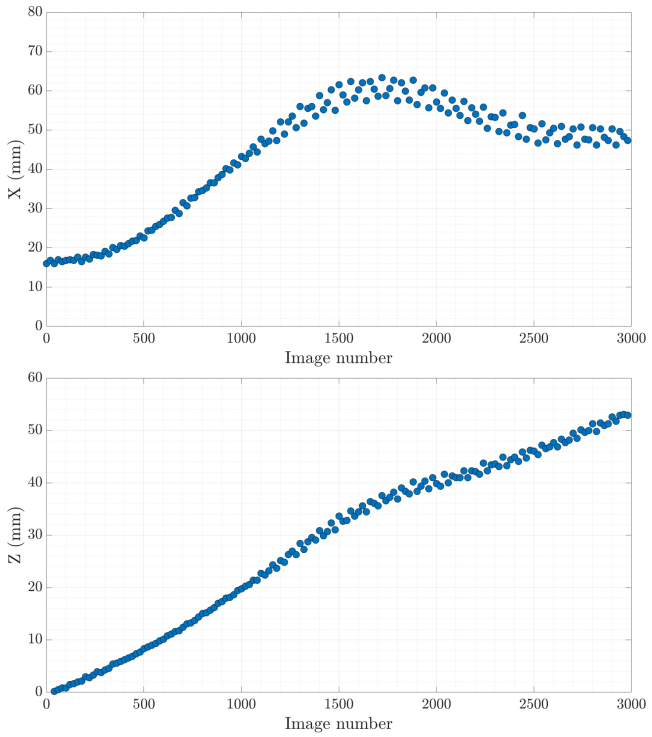

Figure 9: Coordinates of S_2 stagnation point according image number. From top to bottom: X-coordinate and Z-coordinate.

The first one concerns the area below the shock wave of the first sphere. In this region the stagnation point (SP) of the S_2 remains under the shock wave of S_1. As the sphere S_2 rises and the SP point gets closer to the shock wave of S_1, S_2 is pushed farther away in the X-direction. The maximum longitudinal value, X, is reached when the SP of S_2 crosses the shock wave of S_1. At this point, the tendency of the trajectory changes denoting the second behavior when the stagnation point SP of S_2 cross the thick shock wave of the first sphere S_1. As S_2 continuous to rise, its SP gets over the shock wave, but its surface is still in contact with it. S_2 is less and less repulsed in X-direction, which is explained by the decrease of S_1 shock wave impact. After a certain displacement in Z-direction, S_2 is not in contact with S_1 shock wave anymore. One can observed the third behavior, when the sphere S_2 is in the free stream and its trajectory seems to reach a linear path.

As the suspension support of S_2 does not move in X-direction (only in Z-direction), the displacement of the sphere plays a direct role on the angle of its suspension wires. And this angle is the key to calculate forces underwent by S_2 in our swinging sphere experiment, as explained in (3.3).

Regarding the shape of the trajectory, relevant positions of the swinging sphere stagnation point (SP) have been put in evidence and corresponds to inflection points of the trajectory plotted on Figure 10. One another point has been added: the intersection between the shock wave of S_1 and the trajectory of S_2 stagnation point. Those locations will be deeply studied in terms of shock interferences.

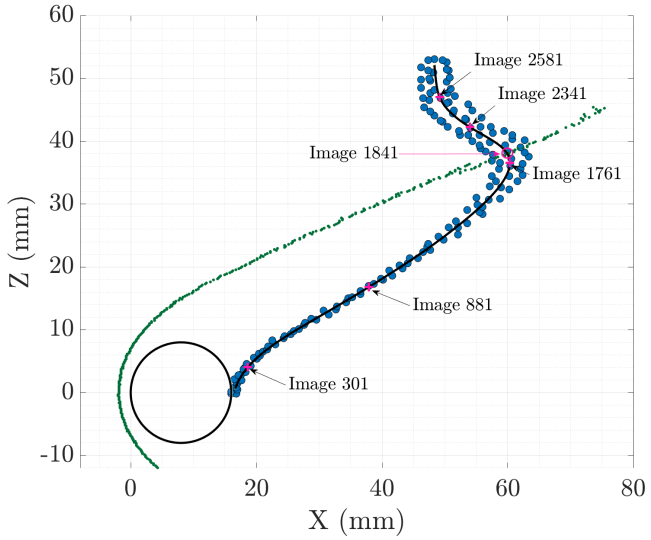

Figure 10: Location of inflection point on the trajectory of S_2 stagnation point.

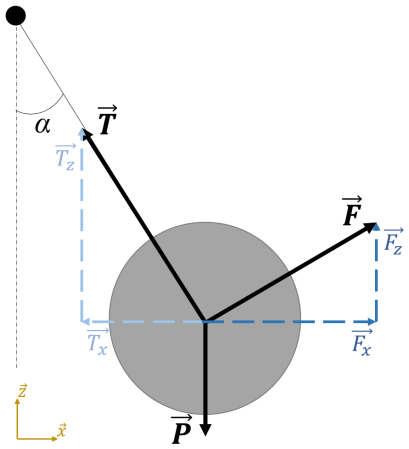

Figure 11: Schematics for the calculation of forces.

3.3. Forces on the swinging sphere

3.3.1. Calculation

For the calculation of forces applied on the sphere S_2, we consider the problem schematized on Figure 11.

The tension of the wire and the weight of the sphere are known and described as follow:

$$\begin{cases} \vec{T} = -T.sin(\alpha).\vec{x} + T.cos(\alpha).\vec{z} \\ \vec{P} = -m.g.\vec{z} \end{cases} \tag{5}$$

Since no difference was measured between the mass of the sphere with or without the wire, the weight of the wire is supposed null. Moreover, the mean free path, or the distance between two molecules of air, is 0.223 mm which is more than three times the diameter of the wires (0.07 mm). Given the low probability for a molecule to collide with the wires, it is considered that no forces are applied on the wires.

Whether S_2 is positioned under or above the shock wave of S_1, it exists transversal forces that attract the sphere in the wake of S_1 or repulsed it far outside the wake. Consequently, S_2 is submitted to drag and lift forces, as shown by Barri [14], Laurence

et al. [15] and Marwege *et al.* [36] in a continuum regime. So, it is supposed that lift forces may exist in a rarefied regime too. The pendulum set-up does not allow to dissociate the drag and lift forces acting on the sphere S_2. However, given the low-density values it is reasonable to assume that the lift forces will be very low. Two hypotheses have been considered to determine the forces applied on S_2 (F_x and F_z represent respectively axial and transversal forces):

a. the sphere is only subjected to axial force:

$$\vec{F} = F_x.\vec{x} \tag{6}$$

b. the sphere is subjected to axial and transversal forces:

$$\vec{F} = F_x.\vec{x} + F_z.\vec{z} \tag{7}$$

In any case, we assume that for each analyzed picture, S_2 is in equilibrium. By application of the fundamental principle of the dynamics ($\sum \vec{Forces} = \vec{F} + \vec{T} + \vec{P} = \vec{0}$, as presented on Figure 11), we obtain the following equations for cases *a* and *b*:

a.

$$\begin{cases} F_x = m.g.tan(\alpha) \\ F_z = 0 \end{cases} \tag{8}$$

b.

$$\begin{cases} F_x = m.g.sin(\alpha) \\ F_z = m.g.(1 - cos(\alpha)) \end{cases} \tag{9}$$

The forces were calculated with the real angle α of the wire of S_2, adjusted from the measured angle, according the bias of the camera, as explained in 3.1.1. Taking into account the accuracy of the angle calculated, forces are given with an accuracy of ±0.18 mN.

The pendulum method was first applied to a single sphere with different diameters in view to determine the forces applied and their drag coefficient. The 16-mm diameter sphere and then an 8-mm diameter sphere made in brass (m = 2.2g) were suspended alone in the well-known free-stream conditions presented in Table 1. Angles were measured for a set of images and forces were calculated with both methods *a* and *b*. The drag coefficient is obtained with Equation 10, where S is the reference area ($S = \pi.D^2/4$).

$$C_d = \frac{F_x}{\frac{1}{2}.\rho_\infty.U_\infty.S} \tag{10}$$

For those two single spheres, values of drag forces and coefficients are given for both methods *a* and *b* in Table 2. Values of the present paper were compared to values compiled from the literature. Indeed, some experiments were carried out in the past to determine aerodynamic coefficient for a single sphere in supersonic and low-density flows. The summary of these values obtained by Aroesty [37], Bailey & Hiatt [38], Kinslow & Potter [39] and Wegener & Ashkenas [40] are plotted on Figure 12 as a function of the similitude parameter Re_{as}, the Reynolds number after a normal shock. As observed, our experimental results look in agreement with the previous works and particularly closer to Aroesty [37] results.

With regards to the applied calculation methods, Figure 12 shows that values from method *a*, *i.e.,* when F_z is supposed inexistent, seem to be a bit high. Wegener & Ashkenas [40], who also experimented a swinging sphere set-up, used method *a* for the calculation of his drag coefficient. Indeed, their free-stream flow is in X-direction only, and their set-up is completed by a floating stabilizer that may compensate movement in Z-direction. But, in our case, the sphere follows a pendulum movement, so the created displacement has components in X and Z directions. Therefore, both forces in X and Z directions must be taken into account, and method *b* seems more appropriate, even-though we do consider the Z-component.

For method *b*, value for the 16 mm-diameter sphere is in a really good agreement with values from the literature, which is less the case for the 8 mm diameter sphere. The drag coefficient value is lightly over-estimated and is almost identical than for *a*. As a reminder, both methods neglect any forces that could act on the wire, in order to approximate forces acting on the sphere. Regarding the 8mm diameter sphere, not only its mass is smaller but also, the forces acting on the sphere are smaller as the surface is divided by four. Nevertheless, the length and diameter of the suspending wires remains the same for both spheres, thus the force acting on the wires are less negligible for the smaller sphere, and may induce an inaccuracy estimating drag forces.

Despite these differences, results from both calculations remain coherent with previous studies, in particular, method *b* seems to give closer values.

In order to estimate the importance of X and Z components of method *b*, the axial and vertical estimated forces are plotted according the image number on Figure 13 from Equation 9. The difference of X and Z components with the modulus of the force ($\|\vec{F}\|$) is quantified. For both the single sphere case (16-mm diameter) and the interfering sphere case, graphs show that the Z component represents 2 to 2.7 % of the modulus of the force. So, the axial component represents the major contribution force, and for this reason we consider the measured axial force as the drag force of the sphere.

For the entire system, composed with one fixed sphere and one swinging sphere, the axial forces were calculated with both methods *a* and *b*. The resulting graph of axial forces are shown on Figure 14 as a function of the relative position between both spheres, represented here by the image numbering.

The maximum difference observed between the two ways to calculate F_x is of 0.5 mN. Considering the fitted curves, the distribution of points gives an accuracy ±0.6 mN at the maximum values of axial forces. This is due to a slight oscillation of the swinging sphere around its equilibrium position. In effect, as we decided not to stop the robot in translation for the entire acquisition of images. Indeed, the time for the sphere to stop oscillating is very long (about 30 minutes), and it would be

Table 2: Drag forces and coefficient for a single sphere

	Calculation method *a*		**Calculation method *b***	
Sphere diameter (mm)	F_x (mN)	C_d	F_x (mN)	C_d
8	2.331 ±0.09	1.554 ±0.06	2.319 ±0.09	1.546 ±0.06
16	8.344 ±0.18	1.390 ±0.04	8.002 ±0.18	1.334 ±0.04

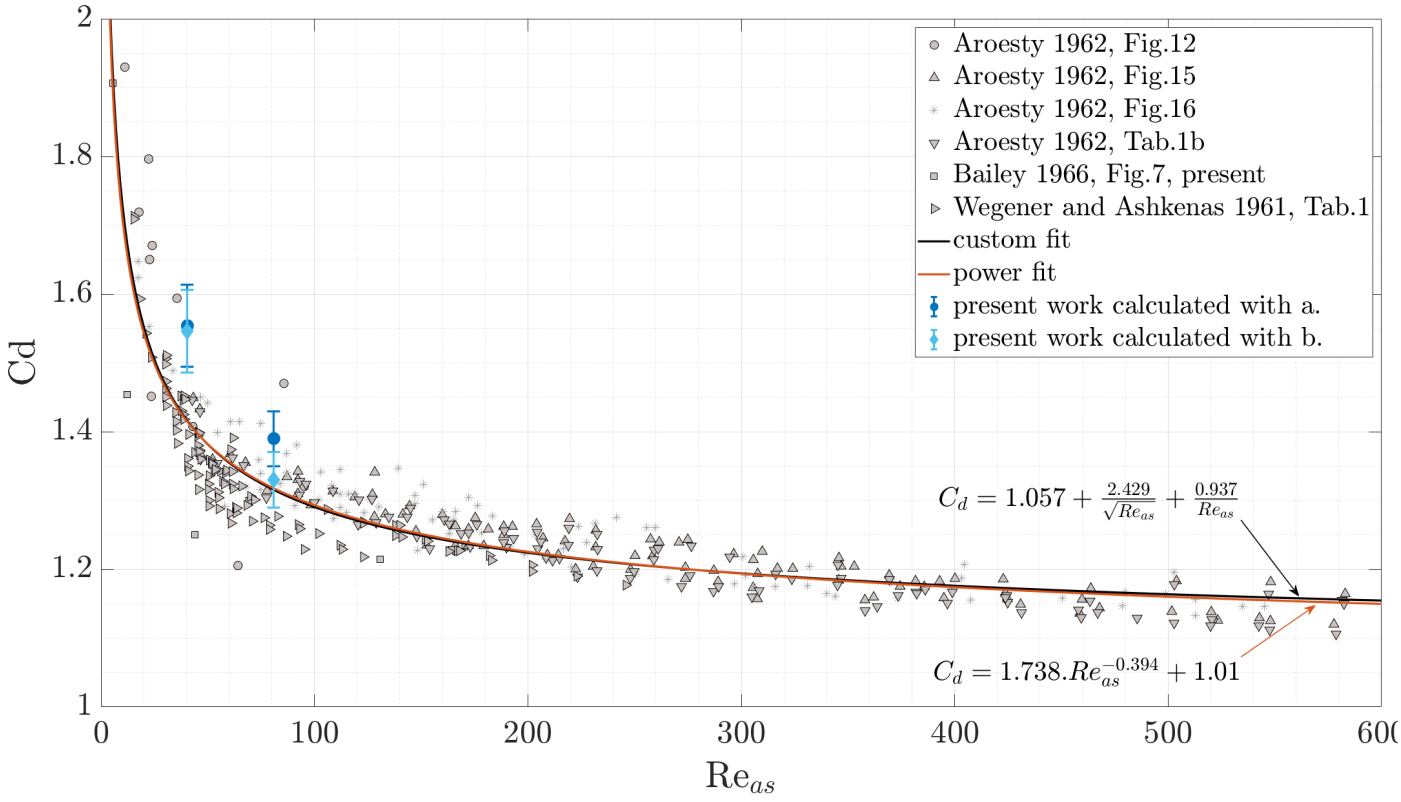

Figure 12: Experimental drag coefficient according the Reynolds number after normal shock.

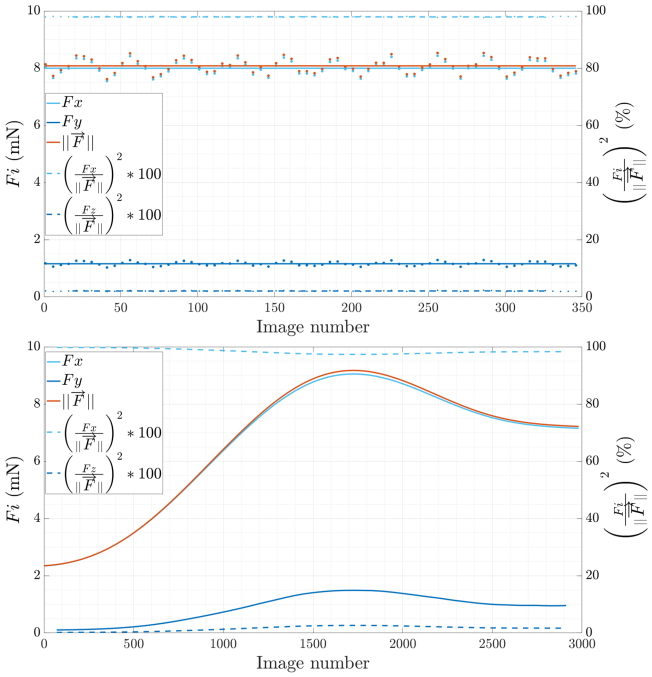

Figure 13: Plot of the forces measured with method *b*. Top graph: forces of one single sphere in the flow. Bottom graph: forces of a sphere behind another one.

impossible to obtain as much values.
In conclusion, method *b* is more representative of the physics, and only the axial force (F_x) is taken into account for the calculation of the drag force.

The drag coefficient of the swinging sphere will not be determined as for this purpose we need values of speed and density of the wake flow of the fixed sphere for each position of the swinging one, and for instance we don't have these values. Nevertheless, the good results obtained with a single sphere, let us think that the general experiment give valid values of drag forces when using method *b*.

3.3.2. Drag forces analysis

For this part, and in light with the previous comments, drag forces will be analyzed considering the axial force (F_x) given in Equation 9. Figure 15 presents the evolution of the drag force of the swinging sphere along its the trajectory, and proposes a link with the shock/shock interferences types following the Edney classification. Inflection points found in 3.2 and plotted in Figure 10 are also presented, along with a series of locations that complete the trajectory. Images shown are the results of the fixed sphere experiment records, on which shock waves have been detected as described in 3.1.2.

First of all, this is interesting to note that, even in initial position, when one can think that S_2 is protected from the flow by S_1, the swinging sphere is submitted to forces, of around 2 mN that pushes it away from the fixed sphere. This brings to light two points concerning: the re-circulation of the flow behind an object in this specific rarefied conditions, and the shape of the wake of the first sphere. Figure 16 shows the flow near a 16 mm-diameter sphere alone in the flow described in Table 1. The image shown is normalized and its colormap has been changed with a jet one in order to enhance contrasts. As it can be observed, the less dense area (cyan to yellow) is very close to the rear of the sphere (less than its half diameter). In initial position of the swinging sphere experiment, S_2 is located just behind S_1. The diameter of S_2 being equal to the diameter of S_1, the surface of the upper front part of the swinging sphere reaches the orange region. This observation, leads to the statement that part of the S_2 surface is in a region where the flow behind the first sphere, even with a very weak density and speed, may induce a pushing force. Secondly, since S_2 is pushed away from S_1, it is very likely to deduce that there is no re-circulation behind S_1. Or, if there is some, the re-circulation region must be small and concentrated on the close rear of S_1, so that an object of the size of S_2 is not influenced by it.
From these observations, for two spherical fragments of same size, with the second just behind the first one, the scenario that can be expected is that the following fragment will not be hidden by the first one for a long duration and both will become single objects.

In a second hand, for the final position, corresponding to image number 3000, the drag force obtained is about 7.16 ±0.18 mN, almost corresponding to the force of a single sphere in the free stream of 8.002 ±0.18 mN. This means that for this position, where S_2 surface is out of S_1 shock region, but where the lower part of S_2 shock wave still crosses the upper part of S_1 shock wave, S_2 seems not to be influenced by the shock/shock interaction anymore. The slight difference in drag force values can be explained by the fact that S_2 is far from the nozzle exit in the X-direction, and close to the radial limit of the nozzle. Eventhough we have 0.85 mN of difference that can be explained by experimental limits, this final value is coherent.

Inflection points of the drag force present some specificities that depends on the position of the second sphere, shock waves shape and shocks interferences. In Figure 17, colormap of those points have been changed to jet in order to enhance contrasts and ease image analysis.
For image number 301, the shock wave of S_2 just begin to penetrate shock wave of S_1. At this point, the sphere begins to be more and more repulsed in X-direction as shock waves begin to slightly interact with each other's. Nevertheless, this interaction still cannot be considered as a type VI interference, as it is the case for the second inflection point illustrated by image number 881, for which the characteristics are described in Cardona *et al.* [20].
As the support of the swinging sphere moves up vertically, drag force continues to increase until the next inflection point: image number 1761. As observed on the graph, this location of S_2 gives the maximal drag force reached by the sphere. One can note that the next important point is image number 1841, where the stagnation point of S_2 encounters the middle of the shock wave of S_1. Those points are linked with a type IV interference which is given as the strongest interaction in continuum regime. Indeed, Bramlette [10], Glass [11], Grasso *et al.* [41], Wieting & Holden [13], and others researchers described type IV interference as the one with the highest heat transfer and

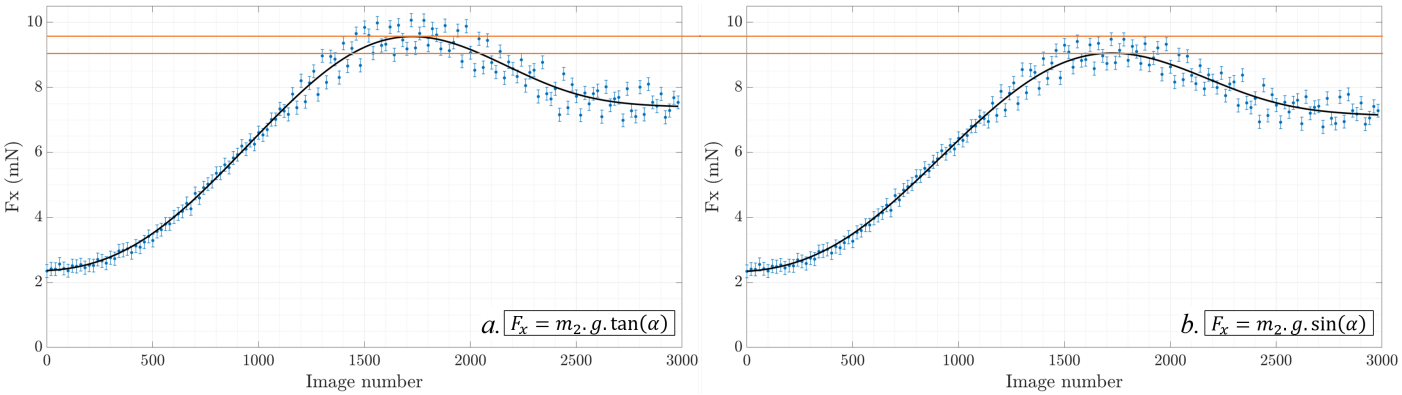

Figure 14: Drag forces according the position of S_2 given with the image number. From left to right, cases *a.* (calculated considering only axial force) and *b.* (calculated considering axial and transversal forces).

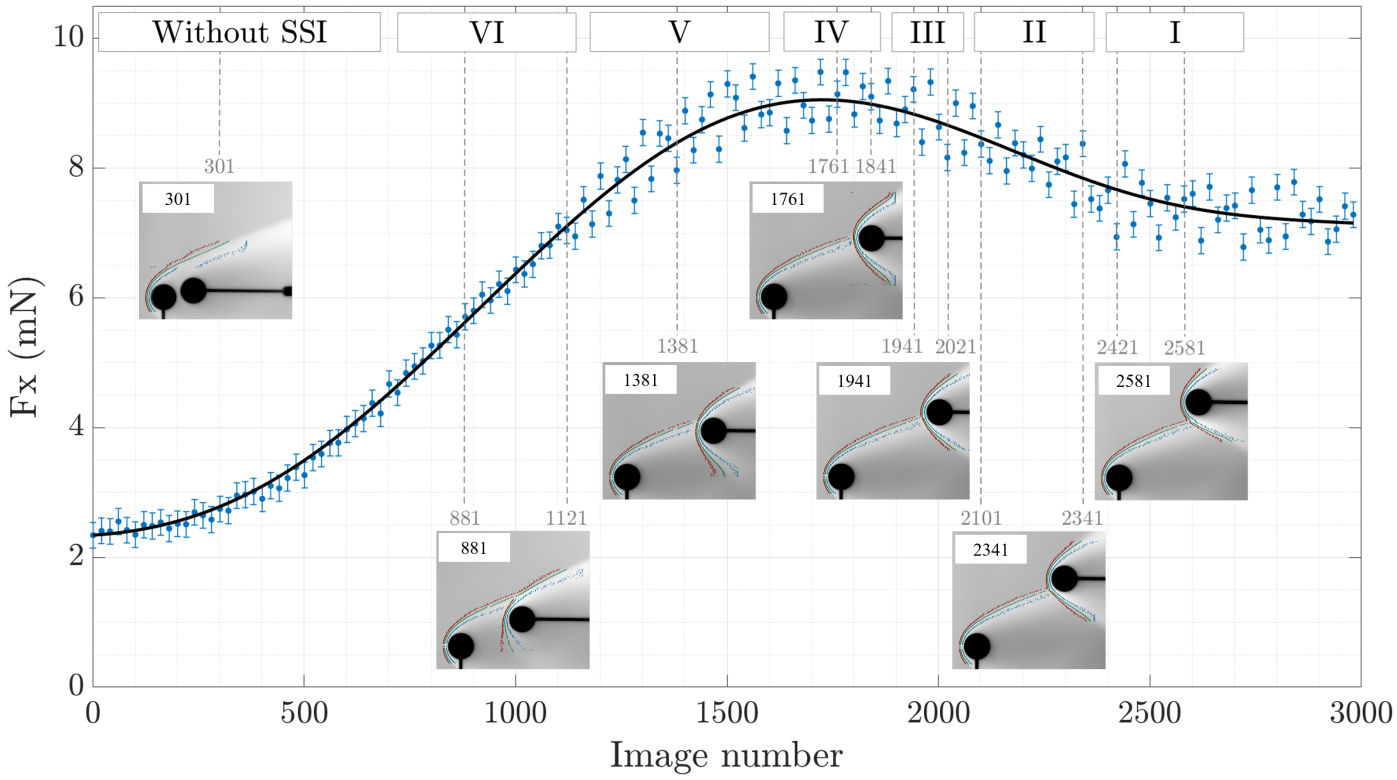

Figure 15: Drag forces according the position of S_2 given with the image number. Superposed images are the result of the fixed sphere experiment identified by shock/shock interferences type.

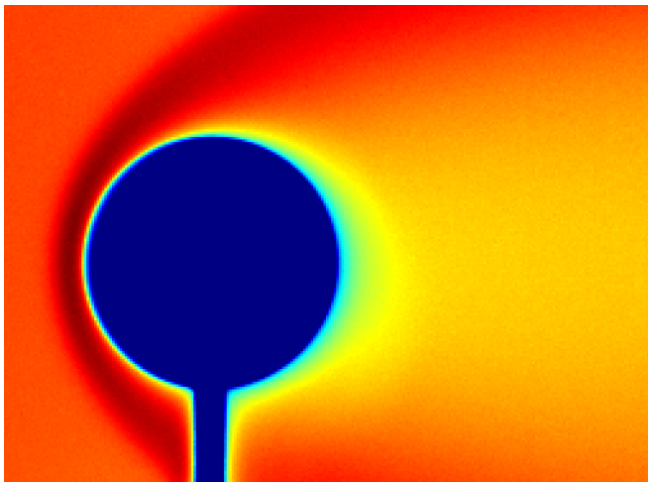

Figure 16: Normalized image of a single sphere with jet colormap.

pressure peaks. For the rarefied regime, questions are examined concerning the existence of type IV interference and the role it plays [42, 21]. As shown with the present level of rarefaction, type IV interferences are observed. In Cardona *et al.* [20], it has not been concluded that this was the strongest interaction due to a lack of evidence. Nevertheless, the present work tends to show the type IV interaction is the most repulsive one, since the drag force reaches a maximum. Thus, it can be expected to observe more important pressure and heat transfer peaks than for the other types.

Once the maximum drag force reached with a type IV shock/shock interference, the stagnation point of S_2 continues its way up above the shock wave of S_1, and the drag force decreases. Shock/shock interference evolves rapidly to a type III and then a type II. Close to the transition between type II and I, at image number 2341, an inflection point is encountered. The drag force begins to decrease less rapidly. It may be a proof that from this distance with the shock wave of S_1, S_2 is less and less affected by the effect of shock/shock interference. The last inflection point (image 2581) gives the end point of the evolution of the drag force. Up to this Z component, the shock/shock interference is no more impacting the flight of the swinging sphere. So S_2 is not under the influence of S_1 anymore even if shock of both spheres interferes with each other. It is to remain that the flow density of this work is very low and shocks are thick but weak, and the unknown is if this behavior occurs at any flow density.

Observing the tendency of the drag force, and with regard to all location studied, we can rank shock/shock interaction according their influence on the second sphere. When the stagnation point is positioned on each side of the shock wave of S_1, the tendency is only increasing or decreasing. The ranking seems logical: the drag force increases so the shock/shock interference is more and more acting on the sphere, and inversely. So, the ranking seems like so: type VI < V < IV and IV > III > II > I. But comparing shock/shock interferences from both sides of the shock wave of S_1 does not seem coherent. Indeed, the plateau values of drag force at the beginning and at the end are not the same, so it would be necessary to rescale both side of the curve to be effective.

4. Conclusion

This experimental study aims to understand the impact of shock/shock interferences on the aerodynamics of a fragment debris flying behind its parent debris. This work focuses on shock/shock interferences occuring in a supersonic rarefied flow when two identical spheres interact with each others.

Experiments were carried out in a Mach 4 steady flow, presenting a static pressure of 2.666Pa, generated in MARHy wind tunnel. The size of both models allow to work in a rarefied regime, with a Knudsen number of 0.0139.

The study consisted in one fixed sphere, and a second sphere suspended in the wake of the first one. As the support of the second sphere was moved up, the second sphere moved in the flow, responding to forces endured, and calculated thanks to the angle made by the suspension wires. The trajectory described by the second sphere, as its support was moved up, was also studied in terms of shock/shock interferences.

It has been shown that the swinging sphere techniques gives drag coefficient in accordance with the literature for one sphere. For two spheres, the quantitative analysis of drag forces showed that, in our case, no recirculation has been seen, and the second sphere cannot be protected by the first sphere from the flow. So, both spheres will eventually stop interacting with each other, whatever their initial positioning. Looking at the value of drag forces and their correspondence in terms of shock/shock interferences, type IV interference happens to be the strongest one in terms of axial repulsion. Comparing interference types in terms of axial repulsion, the following ranking has been proposed : type VI < V < IV and IV > III > II > I.

This study will be completed by an equivalent work for the measure of aerodynamic forces obtained with a another device. It would be interesting to try and calculate the induced drag coefficient in order to add data to the one already existing.

5. Acknowledgments

This work is part of a PhD fully financed by the Agence Nationale de la Recherche for the project IPROF (IPROF: ANR-19-CE39-0003-01) coordinated by Dr. Romain Joussot.

References

[1] ESOC, Esa's annual space environment report gen-db-log-00288-ops-sd, Tech. rep., ESA (2021).
URL https://www.sdo.esoc.esa.int/environment_report/Space_Environment_Report_latest.pdf

[2] S. H. Park, H. D. Kim, G. Park, Orbit, orbital lifetime, and reentry survivability estimation for orbiting objects, Advances in Space Research 62 (11) (2018) 3012–3032. doi:https://doi.org/10.1016/j.asr.2018.08.016.

[3] W. H. Ailor, R. P. Patera, Spacecraft re-entry strategies : meeting debris mitigation and ground safety requirements, Proceedings of the Institution of Mechanical Engineers, Part G: Journal of Aerospace Engineering 221 (6) (2007) 947–953. doi:https://doi.org/10.1243/09544100JAERO199.

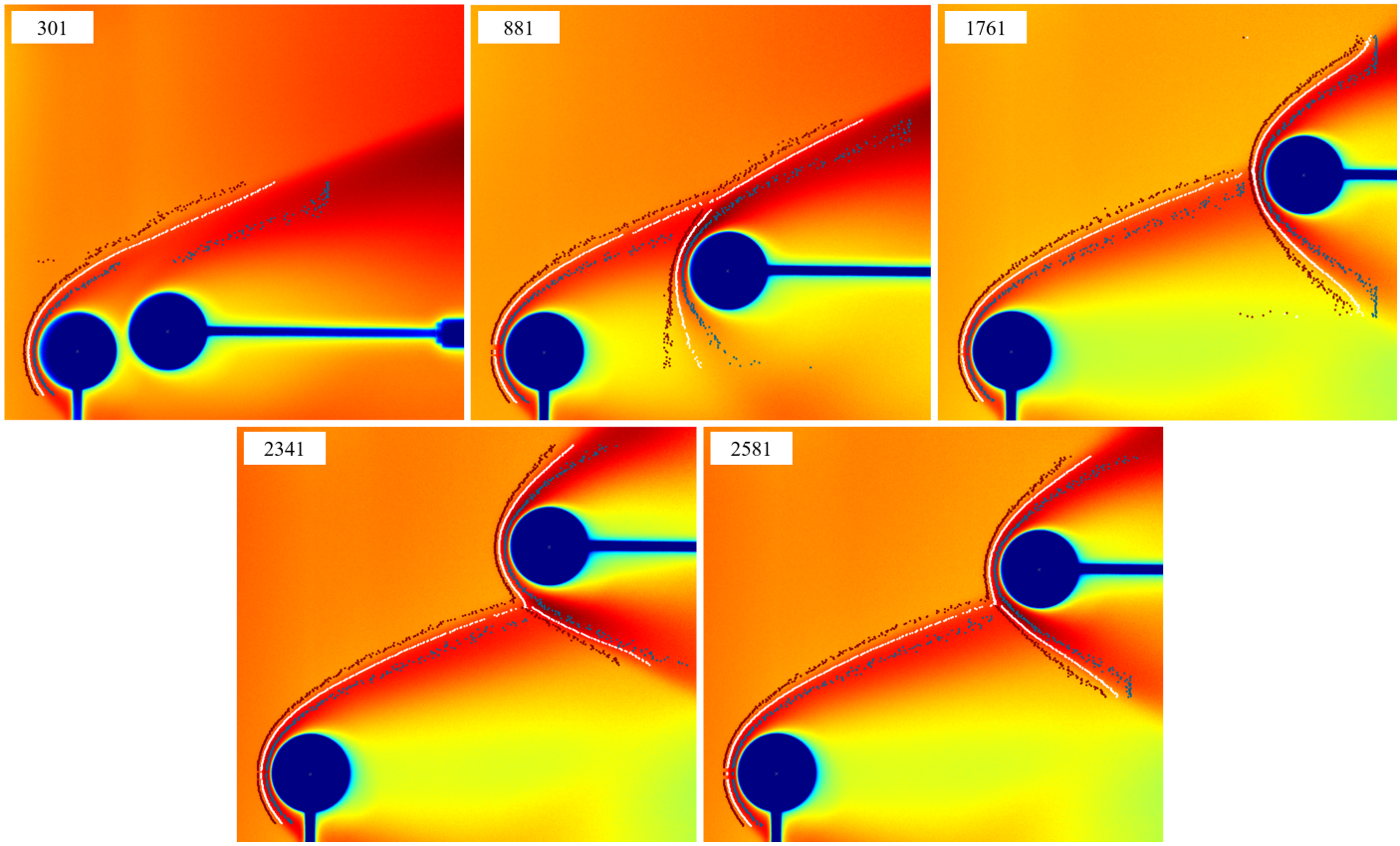

Figure 17: Images of inflection points of the trajectory of S_2 stagnation point with a jet colormap.

[4] S. H. Park, J. N. Laboulais, P. Leyland, S. Mischler, Re-entry survival analysis and ground risk assessment of space debris considering by-products generation, Acta Astronautica (2020). doi:https://doi.org/10.1016/j.actaastro.2020.09.034.

[5] Y. Prevereaud, J. L. Vérant, J. M. Moschetta, F. Sourgen, M. Blanchard, Debris aerodynamic interactions during uncontrolled atmospheric reentry, in: AIAA Atmospheric Flight Mechanics Conference, 2012, p. 4582. doi:https://doi.org/10.2514/6.2012-4582.

[6] C. O. Min, D. W. Lee, Reentry analysis and risk assessment for end-of-life disposal of a multi-layer leo satellite, International Journal of Aeronautical and Space Sciences 19 (2) (2018) 496–508. doi:https://doi.org/10.1007/s42405-018-0036-0.

[7] F. Sanson, On-ground risk estimation of reentering human-made space objects, Phd, Université Paris Saclay (COmUE) (2019).

[8] N. Rembaut, R. Joussot, V. Lago, Aerodynamical behavior of spherical debris in the supersonic and rarefied wind tunnel marhy, Journal of Space Safety Engineering 7 (3) (2020) 411–419. doi:https://doi.org/10.1016/j.jsse.2020.07.031.

[9] B. Edney, Anomalous heat transfer and pressure distributions on blunt bodies at hypersonic speeds in the presence of an impinging shock, Tech. rep., Flygtekniska Forsoksanstalten, Stockholm (Sweden) (1968).

[10] T. T. Bramlette, Simple technique for predicting type iii and iv shock interference, AIAA journal 12 (8) (1974) 1151–1152. doi:https://doi.org/10.2514/3.49435.

[11] C. E. Glass, Numerical simulation of low-density shock-wave interactions, Tech. rep., NASA Langley Research Center (1999).

[12] T. Pot, B. Chanetz, M. Lefebvre, P. Bouchardy, Fundamental study of shock/shock interference in low density flow: flowfield measurements by dlcars, in: RGD : rarefied gas dynamics (Marseille, 26-31 July 1998), 1999, pp. 545–552.

[13] A. R. Wieting, M. S. Holden, Experimental shock-wave interference heating on a cylinder at mach 6 and 8, AIAA Journal 27 (11) (1989) 1557–1565. doi:https://doi.org/10.2514/3.10301.

[14] N. G. Barri, Basic aerodynamical properties of meteoroid fragments in the terrestrial atmosphere, in: AIP Conference Proceedings, Vol. 1283, American Institute of Physics, 2010, pp. 137–144. doi:https://doi.org/10.1063/1.3506048.

[15] S. J. Laurence, R. Deiterding, G. Hornung, Proximal bodies in hypersonic flow, Journal of Fluid Mechanics 590 (2007) 209–237. doi:https://doi.org/10.1017/S0022112007007987.

[16] S. J. Laurence, N. J. Parziale, R. Deiterding, Dynamical separation of spherical bodies in supersonic flow, Journal of fluid mechanics 713 (2012) 159–182. doi:https://doi.org/10.1017/jfm.2012.453.

[17] S. H. Park, J. Kim, I. Choi, G. Park, Experimental study of separation behavior of two bodies in hypersonic flow, Acta Astronautica 181 (2021) 414–426. doi:https://doi.org/10.1016/j.actaastro.2021.01.037.

[18] P. J. Register, M. J. Aftosmis, E. C. Stern, J. M. Brock, P. M. Seltner, S. Willems, A. Guelhan, D. L. Mathias, Interactions between asteroid fragments during atmospheric entry, Icarus 337 (2020) 113468. doi:https://doi.org/10.1016/j.icarus.2019.113468.

[19] V. V. Riabov, A. V. Botin, Numerical and experimental studies of shock interference in hypersonic flows near a cylinder, in: 26th International Congress of the Aeronautical Sciences, Vol. 26, 2008, pp. 1–10.

[20] V. Cardona, R. Joussot, V. Lago, Shock/shock interferences in a supersonic rarefied flow: experimental investigation, Experiments in Fluids 62 (135) (2021). doi:https://doi.org/10.1007/s00348-021-03225-4.

[21] C. White, K. Kontis, The effect of increasing rarefaction on the edney type iv shock interaction problem, in: International Conference on Rail-Newcastel Talks, Springer, Cham, 2018, pp. 299–311. doi:https://doi.org/10.1007/978-3-319-73180-3_23.

[22] M. Ivanov, G. Markelov, S. Gimelshein, Statistical simulation of reactive rarefied flows-numerical approach and applications, in: 7th AIAA/ASME Joint Thermophysics and Heat Transfer Conference, 1998, p. 2669. doi:https://doi.org/10.2514/6.1998-2669.

[23] P. Vashchenkov, A. Kashkovsky, M. Ivanov, Aerodynamics of fragment in spacecraft wake, in: AIP Conference Proceedings, Vol. 663, 2003, pp.

226–233. doi:https://doi.org/10.1063/1.1581554.
[24] G. A. Bird, J. M. Brady, Molecular gas dynamics and the direct simulation of gas flows, Vol. 42, Oxford: Clarendon press, 1994.
[25] I. E. Vas, G. Koppenwallner, The princeton university high pressure hypersonic nitrogen tunnel n-3, Report 690, Princeton University Department of Aerospace and Mechanical Sciences (1964).
[26] G. Koppenwallner, The hypersonic low density wind-tunnel of the aerodynamische versuchsanstalt goettingen-operational behaviour and results on vibrational relaxation, in: 6th Aerospace Sciences Meeting, 1968, p. 49. doi:https://doi.org/10.2514/6.1968-49.
[27] J. K. Harvey, R. W. Jeffery, D. C. Uppington, The imperial college graphite heated hypersonic wind tunnel (1971).
[28] G. P. D. Rajasooria, C. L. Brundin, An experimental investigation of the laminar near wake behind a circular cylinder in a Mach 6, rarefield air stream, University of Oxford, 1970.
[29] V. G. Dulov, V. Y. Levchenko, A. M. Kharitonov, Progress of aerodynamic research at the institute of theoretical and applied mechanics, siberian branch, academy of sciences of the ussr, Journal of Applied Mechanics and Technical Physics 28 (4) (1987) 550–567.
[30] G. A. Bird, Monte-carlo simulation in an engineering context, PrAA 74 (239-255) (1981).
[31] W. Merzkirch, Techniques of flow visualization, Tech. rep., Advisory Group for Aerospace Research and Development, Neuilly-sur-Seine (France) (1981).
[32] S. Coumar, V. Lago, Influence of mach number and static pressure on plasma flow control of supersonic and rarefied flows around a sharp flat plate, Experiments in Fluids 58 (6) (2017) 74. doi:https://doi.org/10.1007/s00348-017-2346-6.
[33] H. Akhlaghi, A. Daliri, M. R. Soltani, Shock-wave-detection technique for high-speed rarefied-gas flows, AIAA Journal 55 (11) (2017) 3747–3756. doi:https://doi.org/10.2514/1.J055819.
[34] S. Cui, Y. Wang, X. Qian, Z. Deng, Image processing techniques in shock-wave detection and modeling, Journal of Signal and Information Processing 4 (3B) (2013) 109. doi:doi:10.4236/jsip.2013.43B019.
[35] Z. Wu, Y. Xu, W. Wang, R. Hu, Review of shock wave detection method in cfd post-processing, Chinese Journal of Aeronautics 26 (3) (2013) 501–513. doi:https://doi.org/10.1016/j.cja.2013.05.001.
[36] A. Marwege, S. Willems, A. Gülhan, M. J. Aftosmis, E. C. Stern, Superposition method for force estimations on bodies in supersonic and hypersonic flows, Journal of Spacecraft and Rockets 55 (5) (2018) 1166–1180. doi:https://doi.org/10.2514/1.A34128.
[37] J. Aroesty, Sphere drag in low density supersonic flow, No. he-150-192, California Univ Berkley Inst of Engineering Research (1962).
[38] A. B. Bailey, Sphere drag measurement in aeroballistics range at high velocities and low reynolds numbers, Tech. rep., ARO INC ARNOLD AFS TN (1966).
[39] M. Kinslow, J. L. Potter, The drag of spheres in rarefied hypervelocity flow, Aedc-tdr-62-205, von Karman Gas Dynamics Facility ARO, Inc. (1962).
[40] P. P. Wegener, H. Ashkenas, Wind tunnel measurements of sphere drag at supersonic speeds and low reynolds numbers, Journal of Fluid Mechanics 10 (4) (1961) 550–560. doi:https://doi.org/10.1017/S0022112061000354.
[41] F. Grasso, C. Purpura, B. Chanetz, J. Délery, Type iii and type iv shock/shock interferences: theoretical and experimental aspects, Aerospace Science and technology 7 (2) (2003) 93–106. doi:https://doi.org/10.1016/S1270-9638(02)00005-6.
[42] V. V. Riabov, A. V. Botin, Shock interference in hypersonic rarefied-gas flows near a cylinder, in: 17th Applied Aerodynamics Conference, 1999, p. 3207. doi:https://doi.org/10.2514/6.1999-3207.

Graphical Abstract

Aerodynamic Forces of Interacting Spheres Representative of Space Debris Re-entry: Experiments in a Supersonic Rarefied Wind-Tunnel⋆

Vincente Cardona, Viviana Lago

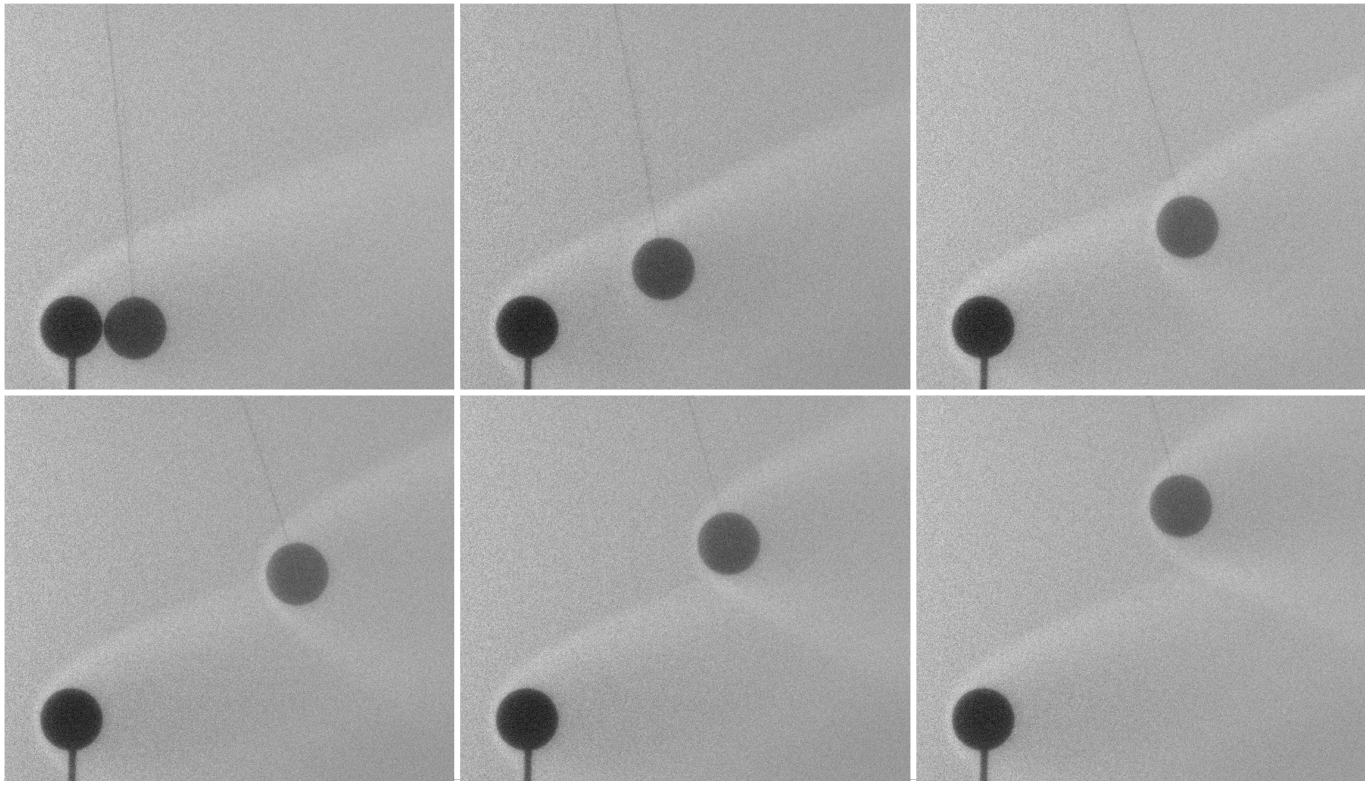

Highlights

Aerodynamic Forces of Interacting Spheres Representative of Space Debris Re-entry: Experiments in a Supersonic Rarefied Wind-Tunnel

Vincente Cardona, Viviana Lago

- Experimental study of relative motion of two interacting spheres in a rarefied flow
- Developed drag measurement technique gives good values for space debris aerodynamics
- In this conditions, two spheres will ultimately stop interacting with each other
- A ranking of the power of shock/shock interference types is proposed
- Type IV interference is the strongest one in terms of axial repulsion force